Journal of Power Sources 186 (2009) 399–407

Contents lists available at ScienceDirect

Journal of Power Sources

journal homepage: www.elsevier.com/locate/jpowsour

Numerical study of thermoelectric characteristics of a planar solid oxide fuel cell with direct internal reforming of methane

Qiusheng Wang[a,*], Lijun Li[b], Cheng Wang[a,b]

[a] School of Civil Engineering and Mechanics, Huazhong University of Science and Technology, Wuhan 430074, China
[b] College of Hydropower and Information Engineering, Huazhong University of Science and Technology, Wuhan 430074, China

ARTICLE INFO

Article history:
Received 22 August 2008
Received in revised form 4 October 2008
Accepted 7 October 2008
Available online 18 October 2008

Keywords:
Planar SOFC
Thermo-fluid model
Internal reforming reaction
Electrochemical kinetic
Thermoelectric characteristic

ABSTRACT

A three-dimensional mathematical thermo-fluid model coupling the electrochemical kinetics with fluid dynamics was developed to simulate the heat and mass transfer in planar anode-supported solid oxide fuel cell (SOFC). The internal reforming reactions and electrochemical reactions of carbon monoxide and hydrogen in the porous anode layer were analyzed. The temperature, species mole fraction, current density, overpotential loss and other performance parameters of the single cell unit were obtained by a commercial CFD code (Fluent) and external sub-routine. Results show that the current density produced by electrochemical reactions of carbon monoxide cannot be ignored, the cathode overpotential loss is the biggest one among the three overpotential losses, and that the proper decrease of the operating voltage leads to the increase of the current density, PEN structure temperature, fuel utilization factor, fuel efficiency and power output of the SOFC.

1. Introduction

Solid oxide fuel cell has been considered as a promising alternative energy source for residential and distributed power plants because of its high energy conversion efficiency and power density, low environmental hazards and potentially low production cost [1]. In addition, internal reforming of natural gas can be performed at the anode, which allows direct use of natural gas as the fuel. For example, the methane is reformed and converted into a mixture of H_2 and CO in the anode of SOFC, which facilitates the electrochemical reaction of H_2 and CO. During this process, thermal gradient across the cell are induced because of the high rate of reforming reactions. Therefore, the internal reforming reaction of hydrocarbons in the SOFC system must be researched and the influence of reforming reaction on the temperature and current density of SOFC also need to be analyzed.

In the past, different SOFC models have been constructed to simulate temperature distribution and current density during the steady operation [2–12]. However, these models only researched the temperature and current density caused by electrochemical reaction of hydrogen. Although Aguiar and Adjiman [13] and Haberman and Young [14] studied the reforming reactions and electrochemical reactions of H_2 and CO, the relationship between the current density produced by the hydrogen oxidation reaction and the carbon monoxide oxidation reaction was not analyzed. Therefore, it is necessary to probe into the physical mechanisms, and the effects of the electrochemical and the reforming reactions on the distribution of temperature and current density during the operating process of SOFC.

The paper developed a comprehensive mathematical model on the basis of our original study [15,16] to simulate the reforming reactions in the anode and predict the temperature distribution, current density and overpotential. Moreover, The paper also simulated the influence of the operating conditions on the temperature and current density of SOFC to improve the performance of SOFC. Lastly, comparisons of current-power density and current-fuel efficiency variations in a H_2–H_2O system and a CO–CO_2 system was accomplished to analyze the effect of water-shift reaction on the performance of SOFC.

2. Mathematical model description

A solid oxide fuel cell (SOFC) consists of an interconnect structure and a three-layer region composed of two ceramic electrodes, anode and cathode, separated by a dense ceramic electrolyte (often referred to as the PEN-positive-electrode/electrolyte/negative-electrode). Structure of a schematic drawing of the SOFC unit is shown in Fig. 1. The SOFC cell unit geometries are given as follows

* Corresponding author at: Department of Mechanics, Huazhong University of Science and Technology, Wuhan 430074, Hubei, China. Tel.: +86 27 62044772; fax: +86 27 87544644x22.
E-mail address: wangqiusheng_hust@yahoo.com.cn (Q. Wang).

0378-7753/$ – see front matter © 2008 Elsevier B.V. All rights reserved.
doi:10.1016/j.jpowsour.2008.10.034

Nomenclature

A	activation energy ($J\,mol^{-1}$)
B	inertial coefficient
C_p	specific heat at constant pressure ($J\,kg^{-1}\,K^{-1}$)
$D_{i,eff}$	effective diffusion coefficient of species i ($m^2\,s^{-1}$)
$D_{i,m}$	molecular diffusion coefficient of species i ($m^2\,s^{-1}$)
D_{Ki}	Knudsen diffusion coefficient of species i ($m^2\,s^{-1}$)
E	electromotive force (V)
$\bar{E}$	equivalent voltage (V)
F	Faraday constant ($C\,mol^{-1}$)
ΔG	change of Gibbs free enthalpy ($kJ\,mol^{-1}$)
Δh	enthalpy change ($kJ\,mol^{-1}$)
h_a	anode thickness (mm)
h_c	cathode thickness (μm)
h_e	electrolyte thickness (μm)
i	local current density ($A\,m^{-2}$)
Δi	current density difference ($A\,m^{-2}$)
J_i	mass flux of species i ($kg\,m^{-3}\,s^{-1}$)
k	reaction rate constant ($mol\,m^{-3}\,Pa^{-2}\,s^{-1}$)
K	permeability coefficient (m^2)
K_e	equilibrium constants (Pa^2)
L	cell length (mm)
M_i	molecular weight of component i ($kg\,mol^{-1}$)
M_m	average molecular weight ($kg\,mol^{-1}$)
n_a	air channel inlet flow rate ($mol\,h^{-1}$)
n_f	fuel channel inlet flow rate ($mol\,h^{-1}$)
p	pressure (Pa)
p_i	partial pressure of component i (Pa)
P_{SOFC}	power density of the cell ($W\,m^{-2}$)
Q	lower heating value
R	gas constant ($J\,mol^{-1}\,K^{-1}$); reaction rate ($mol\,m^{-3}\,s^{-1}$); Ohmic resistivity (Ωm)
S	source term
S_i	species source
S_m	mass source
S_T	energy source
S_v	momentum source
T	temperature (K)
ΔT	temperature difference of the PEN structure (K)
U_{fuel}	fuel utilization factor
v_k	velocity components in k direction ($m\,s^{-1}$)
$\mathbf{V}$	velocity vector ($m\,s^{-1}$)
V_{cell}	operating voltage (V)
W	cell width (mm)
y	molar fraction
Y	mass fraction of species
Z	temperature variable

Greak letters

α_{im}	molar coefficient
ε	porosity
ε_{SOFC}	fuel efficiency
η	overpotential (V)
$\kappa_{i,eff}$	effective thermal conductivity ($W\,m^{-1}\,K^{-1}$)
λ_{air}	air ratio
μ_{eff}	effective dynamic viscosity ($kg\,m^{-1}\,s^{-1}$)
ρ	density ($kg\,m^{-3}$)
σ	electrical conductivity ($\Omega^{-1}\,m^{-1}$)
τ	tortuosity

Subscripts

a	anode
air	air gas channel
ave	average value
c	cathode
co–oxy	reaction of carbon monoxide and oxygen
CO	carbon monoxide
CO_2	carbon dioxide
CH_4	methane
e	electrolyte
fuel	fuel gas channel
H_2;hyd	hydrogen
H_2O	stream
hyd–oxy	reaction of hydrogen and oxygen
k	x, y, and z directions in Cartesian coordinates
max	maximum value
min	minimum value
O_2;oxy	oxygen
r	steam reforming reaction
s	water–gas shift reaction

Superscripts

in	feed conditions (fuel and air channel inlet)
out	feed conditions (fuel and air channel outlet)
0	standard pressure
+	forward reaction
−	reverse reaction

[17]: anode thickness $h_a = 2$ mm, electrolyte thickness $h_e = 20$ μm, and cathode $h_c = 50$ μm. The U, V and W are the velocity components in the x, y and z directions, respectively.

2.1. Governing equations and source terms

The governing equations to be solved are the continuity, momentum, energy and species equations. The mass continuity equation is written as

$$\nabla \cdot (\varepsilon \rho \mathbf{V}) = S_m \tag{1}$$

where ε, ρ and $\mathbf{V}$ are the porosity of porous electrodes, the effective density of the multi-component gas mixture and velocity vector, respectively. S_m is the source term, which describes the change of species mass caused by electrochemical reactions at the reaction layers next to the interfaces between electrolyte and porous

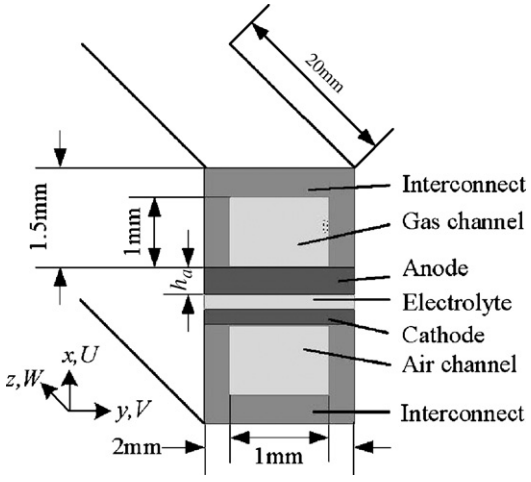

Fig. 1. Schematic drawing of a SOFCs cell unit.

electrodes.

$$S_m = \sum J_i \tag{2}$$

where J_i is the mass flux of species i during the electrochemical reaction process. In the fuel channel and air channel, $\varepsilon = 1$ and $S_m = 0$. In the anode and cathode, $\varepsilon = 0.46$.

The momentum equation is as follows:

$$\nabla \cdot (\varepsilon \rho \mathbf{VV}) = -\varepsilon \nabla p + \nabla \cdot (\varepsilon \mu_{\text{eff}} \nabla \mathbf{V}) + S_v \tag{3}$$

where p and μ_{eff} are the pressure and the effective dynamic viscosity, respectively. S_v is the momentum source in the porous electrodes, and can be calculated by the following formula:

$$S_v = -\left(\frac{\mu_{\text{eff}} \mathbf{V}}{K + \varepsilon \rho B v_k |\mathbf{V}|}\right) \tag{4}$$

where K is the porous electrode permeability, and v_k is the velocity component in the k direction. The first term on the right side of Eq. (4) accounts for the linear relationship between the pressure gradient and flow rate on the basis of the Darcy's law. The second term is the Forchheimer term which takes into account the inertial force effects [18]. In the fuel channel and air channel, $\varepsilon = 1$ and $S_v = 0$. In the anode and cathode, $\varepsilon = 0.46$.

The species conservation equation is:

$$\nabla \cdot (\varepsilon \rho Y_i \mathbf{V}) = \nabla \cdot (\rho D_{i,\text{eff}} \nabla Y_i) + S_i \tag{5}$$

where Y_i is the mass fraction of species i; $D_{i,\text{eff}}$ is the effective gas diffusion coefficient of species i in the porous electrodes and fluid channels. Based on the dusty-gas model (DGM) [17,19] used in this paper, $D_{i,\text{eff}}$ in the porous electrodes can be expressed as follows:

$$D_{i,\text{eff}} = \frac{\varepsilon}{\tau}\left(\frac{1 - \alpha_{\text{im}} y_i}{D_{i,m}} + \frac{1}{D_{\text{Ki}}}\right)^{-1} \tag{6}$$

where τ is the tortuosity, $D_{i,m}$ is the molecular diffusion coefficient of the species i, y_i is the molar fraction of the species i, and D_{Ki} is the Knudsen diffusion coefficient of species i. Here, α_{im} is defined as follows:

$$\alpha_{\text{im}} = 1 - \left(\frac{M_i}{M_m}\right)^{0.5} \tag{7}$$

where M_i is the molecular weight of species i, and M_m is average molecular weight. S_i is the production/consumption rate of species i as a result of reforming reactions and electrochemical reactions. In the fuel channel and air channel, $\varepsilon = 1$ and $S_i = 0$. In the anode and cathode, $\varepsilon = 0.46$.

The energy equation can be expressed as

$$\nabla \cdot (\rho C_p \mathbf{V} T) = \nabla \cdot (\kappa_{i,\text{eff}} \nabla T) + S_T \tag{8}$$

where C_p, $\kappa_{i,\text{eff}}$, T, and S_T are specific heat at constant pressure, the effective thermal conductivity, temperature, and the heat source term, respectively. In the fuel channel, air channel and interconnect, $S_T = 0$.

2.2. Reforming and electrochemical reactions

In this paper, the fuel is a mixture of hydrogen (H_2), steam (H_2O), carbon monoxide (CO), carbon dioxide (CO_2), and methane (CH_4). The reforming reactions in the anode of this case are described by the following two reaction equations:

$$CH_4 + H_2O \leftrightarrow 3H_2 + CO$$

$$\Delta h_T = 192.220 + 0.0541T - 2.062 \times 10^{-5} T^2 \quad (\text{kJ mol}^{-1}) \tag{9}$$

$$CO + H_2O \leftrightarrow H_2 + CO_2$$

$$\Delta h_T = -44.034 + 0.00847T - 5.819 \times 10^{-7} T^2 \quad (\text{kJ mol}^{-1}) \tag{10}$$

In the whole paper, Δh_T is the enthalpy change of reactions, which is the function of the local temperature [20]. Steam reforming reaction described by Eq. (9) is strongly endothermic. In contrast, the water–gas shift reaction described by Eq. (10) is weakly exothermic.

Electrochemical processes on the cathode and anode can be expressed as follows:

$$\tfrac{1}{2}O_2 + 2e^- \rightarrow O^{2-} \text{ (cathode)} \tag{11}$$

$$H_2 + O^{2-} \rightarrow H_2O + 2e^- \quad \text{(anode)} \tag{12}$$

$$CO + O^{2-} \rightarrow CO_2 + 2e^- \quad \text{(anode)} \tag{13}$$

The overall electrochemical reactions are thus described as follows:

$$H_2 + \tfrac{1}{2}O_2 \rightarrow H_2O$$

$$\Delta h_T = -238.376 - 0.0124T + 3.036 \times 10^{-6} T^2 \,(\text{kJ mol}^{-1}) \tag{14}$$

$$CO_2 + \tfrac{1}{2}O_2 \rightarrow CO_2$$

$$\Delta h_T = -283.838 - 0.00137T + 2.500 \times 10^{-6} T^2 \,(\text{kJ mol}^{-1}) \tag{15}$$

These electrochemical reactions of hydrogen, Eq. (14), and carbon monoxide, Eq. (15), are exothermic.

2.3. Internal reforming reaction kinetics

It is common to employ the forward kinetic reforming reactions in the following form:

$$k^+ = k_0 f(p_0) \exp\left(\frac{-E_a}{RT}\right) \tag{16}$$

where k^+ is the forward reaction rate constant, f is the function of the species partial pressure, while E_a stands for the activation energy, and k_0 is the pre-exponential constant. It is revealed that the first order kinetic expression is considered to be typical of direct internal reforming reaction in SOFC performance. Arrhenius curves fit to the date of Lehnert et al. [21] are adopted in this study:

$$k_r^+ = 2169 \exp\left(\frac{-225103}{RT}\right) \tag{17}$$

$$k_s^+ = 0.0183 \exp\left(\frac{-103842}{RT}\right) \tag{18}$$

where k_r^+ and k_s^+ are the forward reaction rate constants of reactions (9) and (10), respectively. The backward reaction rate constants of reactions (9) and (10), k_r^- and k_s^-, can be determined based on the following equilibrium constants K_e for the two reactions

$$K_{er} = \frac{k_r^+}{k_r^-} \tag{19}$$

$$K_{es} = \frac{k_s^+}{k_s^-} \tag{20}$$

K_{er} and K_{es} are the equilibrium constants of reactions (9) and (10), which can be calculated by the following empirical equations [14,18]:

$$K_{er} = 1.0267 \times 10^{10} \exp(-0.2513Z^4 + 0.3665Z^3 + 0.5810Z^2 - 27.134Z + 3.2770) \tag{21}$$

$$K_{es} = \exp(-0.2935Z^3 + 0.6351Z^2 + 4.1788Z + 0.3169) \quad (22)$$

$$Z = \frac{1000}{T - 1} \quad (23)$$

The volumetric reaction rates of reactions (9) and (10), R_r and R_s, can be defined as follows:

$$R_r = k_r^+ p_{CH_4} p_{H_2O} - k_r^- p_{CO} (p_{H_2})^3 \quad (24)$$

$$R_s = k_s^+ p_{CO} p_{H_2O} - k_s^- p_{CO_2} p_{H_2} \quad (25)$$

where p_i is partial pressure of species i. Then, S_i in Eq. (5) as a result of the reforming reactions reads:

$$S_{H_2} = (3R_r + R_s)M_{H_2}, \quad S_{CH_4} = -R_r M_{CH_4},$$
$$S_{H_2O} = (-R_r - R_s)M_{H_2O}, \; S_{CO} = (R_r - R_s)M_{CO} \quad (26)$$

S_T in Eq. (8) as a result of the reforming reactions reads:

$$S_T = -R_r \Delta h_r - R_s \Delta h_s \quad (27)$$

In which, Δh_r and Δh_s are the enthalpy changes in reactions (9) and (10), respectively.

2.4. Electrochemical model

The electrochemical reactions of hydrogen and carbon monoxide, described by Eqs. (14) and (15), respectively, are considered in the present model. The electromotive forces, E, generated by those reactions, are calculated locally by the Nernst equation:

$$E_{hyd-oxy} = E^0_{hyd-oxy} + \frac{RT}{2F} \ln\left(\frac{p_{H_2}(p_{O_2}/100000)^{0.5}}{p_{H_2O}}\right) \quad (28)$$

$$E_{co-oxy} = E^0_{co-oxy} + \frac{RT}{2F} \ln\left(\frac{p_{CO}(p_{O_2}/100000)^{0.5}}{p_{CO_2}}\right) \quad (29)$$

where

$$E^0_{hyd-oxy} = \frac{\Delta G^0_{hyd-oxy}}{2F} = 1.271 - 2.731 \times 10^{-4} T \quad (30)$$

$$E^0_{co-oxy} = \frac{\Delta G^0_{co-oxy}}{2F} = 1.474 - 4.679 \times 10^{-4} T \quad (31)$$

The subscripts "hyd–oxy" and "co–oxy" indicate the H_2 and CO oxidation reactions (14) and (15), respectively. $\Delta G^0_{hyd-oxy}$ and ΔG^0_{co-oxy} are the changes of the standard Gibbs free energy for each reaction, which are locally estimated as the functions of the local cell temperature [20]. F is the Faraday constant.

The overpotentials, η, accompanied with the sluggishness of each reaction of Eqs. (11)–(13) to occur in the electrodes, are calculated with the following empirical equations suggested by Achenbach [22]:

$$\eta_{hyd} = i_{hyd-oxy}\left(\frac{2F}{RT} k_{hyd}\left(\frac{p_{H_2}}{p_{fuel}}\right)^{0.25} \exp\left(\frac{-A_a}{RT}\right)\right)^{-1} \quad (32)$$

$$\eta_{co} = i_{co-oxy}\left(\frac{2F}{RT} k_{co}\left(\frac{p_{CO}}{p_{fuel}}\right)^{0.25} \exp\left(\frac{-A_a}{RT}\right)\right)^{-1} \quad (33)$$

$$\eta_{oxy} = (i_{hyd-oxy} + i_{co-oxy})\left(\frac{4F}{RT} k_{oxy}\left(\frac{p_{O_2}}{p_{air}}\right)^{0.25} \exp\left(\frac{-A_c}{RT}\right)\right)^{-1} \quad (34)$$

where η_{hyd} and η_{co} are the anode overpotential losses. η_{oxy} is the cathode overpotential loss. $i_{hyd-oxy}$ and i_{co-oxy} are the local electric current densities produced by the oxidation reactions (14) and (15), respectively. Electric current is assumed to flow only in y direction in the electrolyte and the electrodes. The coefficients k_{hyd}, k_{co}, and k_{oxy} are given as $k_{hyd} = 2.13 \times 10^8\ A\,m^{-2}$, $k_{co} = 2.98 \times 10^8\ A\,m^{-2}$, and $k_{oxy} = 1.49 \times 10^{10}\ A\,m^{-2}$. A_a and A_c are the activation energy: $A_a = 1.1 \times 10^5\ J\,mol^{-1}$ and $A_c = 1.6 \times 10^5\ J\,mol^{-1}$.

Ohmic resistivities of the electrolyte and electrodes of the cell are also locally calculated. In the present model, the following empirical formulae suggested by Ferguson [12] are adopted to evaluate their temperature dependency:

$$\sigma_e = 3.34 \times 10^4 \exp\left(\frac{-10300}{T}\right) \quad (35)$$

$$\sigma_c = \frac{4.2 \times 10^7}{T} \exp\left(\frac{-1200}{T}\right) \quad (36)$$

$$\sigma_a = \frac{9.5 \times 10^7}{T} \exp\left(\frac{-1150}{T}\right) \quad (37)$$

In which, σ_e is the oxide ionic conductivity of the electrolyte while σ_c and σ_a are the electric conductivity of the cathode and anode, respectively.

Here the following local relations exist among the electromotive force E, overpotential loss η, current density i, and electric potentials of cathode and anode, V_c and V_a:

$$E_{hyd-oxy} - (\eta_{hyd} + \eta_{oxy} + \eta_{ohm}) = V_c - V_a \quad (38)$$

$$E_{co-oxy} - (\eta_{co} + \eta_{oxy} + \eta_{ohm}) = V_c - V_a \quad (39)$$

where

$$\eta_{ohm} = i(R_e h_e + R_c h_c + R_a h_a), \quad i = i_{hyd-oxy} + i_{co-oxy},$$
$$R_e = \frac{1}{\sigma_e}, \quad R_c = \frac{1}{\sigma_c}, \quad R_a = \frac{1}{\sigma_a} \quad (40)$$

R_e, R_c and R_a are the ohmic resistivity of the electrolyte, cathode and anode, respectively. From the above relations, we can obtain the local current density i if the local potential difference $V_c - V_a$ is given, and *vice versa*. In the present model, the cell terminal voltage defined as $V_{cell} = V_c - V_a$ is given as a condition to start the computation for one operating condition (called operating voltage), and thereby both the current densities and potential fields are calculated based on an equivalent electrical circuit model illustrated in Fig. 2.

The mass production/consumption rate of each chemical species, S_i in Eq. (5), is related to the local current density produced by the electrochemical reactions.

$$S_{H_2} = \frac{i_{hyd-oxy} M_{H_2}}{2F}, \quad S_{H_2O} = \frac{i_{hyd-oxy} M_{H_2O}}{2F}, \quad S_{CO} = \frac{-i_{co-oxy} M_{CO}}{2F},$$
$$S_{CO_2} = \frac{-i_{co-oxy} M_{CO_2}}{2F}, \quad S_{O_2} = \frac{(-i_{hyd-oxy} + i_{co-oxy}) M_{O_2}}{4F}, \quad (41)$$

Table 1
Performance factors of the cell.

Fuel utilization factor $U_{fuel} = \frac{i_{ave} LW}{(8Fy^{in}_{CH_4} + 2Fy^{in}_{H_2} + 2Fy^{in}_{CO})n_f}$	(45)
Air ratio $\lambda_{air} = \frac{y^{in}_{O_2} n_a}{i_{ave} LW/4F}$	(46)
Power density $P_{SOFC} = i_{ave} V_{cell}$	(47)
Fuel efficiency $\varepsilon_{SOFC} = \frac{i_{ave} V_{cell} LW}{(y^{in}_{CH_4} Q^{in}_{CH_4} + y^{in}_{H_2} Q^{in}_{H_2} + y^{in}_{CO} Q^{in}_{CO})n_f}$	(48)

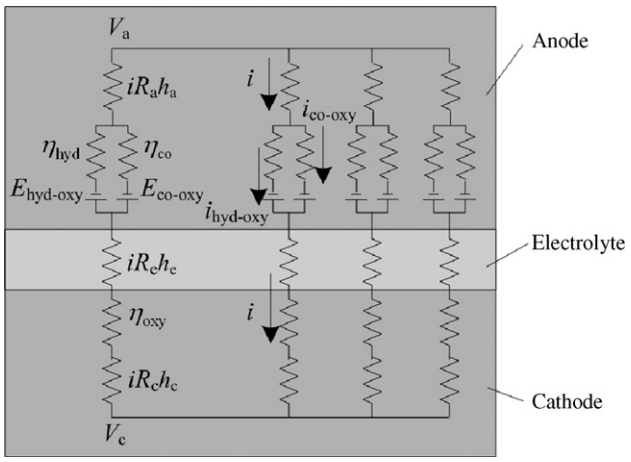

Fig. 2. Equivalent electrical circuit in the cell.

Based on the local current densities obtained, thermodynamic heat (except the ohmic heat) generation by the electrochemical reactions in Eq. (8) is calculated as follows:

$$S_T = \left(\frac{-\Delta h_{hyd-oxy}}{2F-\bar{E}}\right) i_{hyd-oxy} + \left(\frac{-\Delta h_{co-oxy}}{2F-\bar{E}}\right) i_{co-oxy} \quad (42)$$

where

$$\bar{E} = E_{hyd-oxy} - (\eta_{hyd} + \eta_{oxy}) = E_{co-oxy} - (\eta_{co} - \eta_{oxy}) \quad (43)$$

$\Delta h_{hyd-oxy}$ and Δh_{co-oxy} are the enthalpy changes for each of the reactions (14) and (15), respectively. Ohmic heating in the electrolyte or in the electrodes is also locally calculated based on the ohmic resistivities and current densities. In the anode, cathode and electrolyte, the ohmic heat is calculated as follows:

$$S_T = i^2 R_j h_j \quad j \in \{a, c \text{ and } e\} \quad (44)$$

2.5. Model performance factors

The fuel utilization factor is the fraction of the total inlet fuel used to produce electricity in the cell. The air ratio reflects the excess air, in relation to that which is stoichiometrically needed, that is supplied to the cell for cooling. Table 1 presents the mathematical definition of these performance factors.

Where i_{ave} is the average total current density. L and W are the cell length and cell width. n_a and n_f are air channel inlet flow rate and fuel channel inlet flow rate. Q is lower heating value. The superscript *in* denotes feed conditions (fuel and air channel inlet).

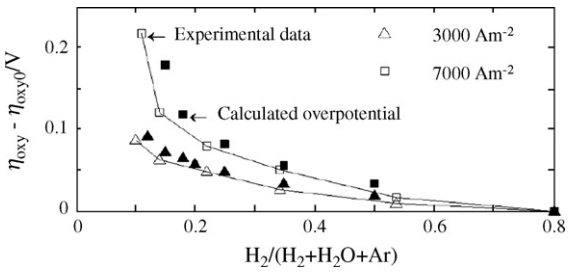

Fig. 3. Comparison between the calculated overpotential and experimental data for the H_2–H_2O–Ar system.

2.6. Validation

In order to validate the numerical model described above, we compare the cathode overpotential loss predicted by the simulation with the experimental data reported by Suwanwarangkul et al. [23]. Fig. 3 presents the comparison between the calculated cathode overpotential loss and experimental data for the H_2–H_2O–Ar system described in the reference. A good agreement is found between the calculated results and experimental data.

3. Results and discussion

The SOFC parameters appeared in the literature are applied as a base case in this study. Fuel and air inlet conditions are: temperature T_{in} = 1173 K. The inlet fuel is considered as a gas mixture of H_2, CH_4, CO, H_2O, and CO_2. This gas mixture is produced by a mixture of H_2O/CH_4 = 2.5 after 30% pre-reforming at CO shift equilibrium, and the steam content is 26.3% in H_2, 17.1% in CH_4, 2.9% in CO, 49.3% in H_2O, and 4.4% in CO_2. The molar composition of the air is 21% O_2 and 79% N_2. Hydrogen and carbon monoxide are used as the fuel in the H_2–H_2O system and CO–CO_2 system.

The governing Eqs. (1), (3), (5) and (8), together with the boundary conditions and initial conditions are solved with computational fluid dynamics software FLUENT by finite volume method. The modeling domain consists of the fuel channel, air channel, interconnect and PEN structure. The computation including direct internal reforming of methane is carried out for the three cases shown in Table 2. The computation for the H_2–H_2O system and CO–CO_2 system is carried out for the two cases shown in Table 7. Solid material properties used in the simulation for all the cases are listed in Table 3.

Figs. 4–7 show the predicted results for case1 given in Table 2. Fig. 4 shows the mole fraction profiles of all the species in the fuel channel and the total current density profile along the cell length direction. These illustrate the impact of the simultaneous reactions of the direct internal reforming reaction, the water–gas shift reaction, and the oxidation reactions of H_2 and CO at the anode/electrolyte interface. At the entrance of the fuel cell, due to

Table 2
Computational parameters and results for three calculated cases [24].

Cases	Flow	Inlet gas delivery		Inlet temperature		Fuel inlet composition					Air inlet composition	
	Pattern	n_f^{in} (mol h^{-1})	n_a^{in} (mol h^{-1})	T_{air}^{in} (K)	T_{fuel}^{in} (K)	$y_{CH_4}^{in}$	$y_{H_2O}^{in}$	y_{CO}^{in}	$y_{H_2}^{in}$	$y_{CO_2}^{in}$	$y_{O_2}^{in}$	$y_{N_2}^{in}$
1,2,3	Co-flow	3.05E−3	3.81E−2	1173	1173	0.171	0.493	0.029	0.263	0.044	0.21	0.79
Cases	Operating	Outlet gas delivery		Outlet temperature		Fuel outlet composition					Air outlet composition	
	Voltage (V)	n_f^{out} (mol h^{-1})	n_a^{out} (mol h^{-1})	T_{air}^{out} (K)	T_{fuel}^{out} (K)	$y_{CH_4}^{out}$	$y_{H_2O}^{out}$	y_{CO}^{out}	$y_{H_2}^{out}$	$y_{CO_2}^{out}$	$y_{O_2}^{out}$	$y_{N_2}^{out}$
1	0.682	4.10E−3	3.68E−2	1194	1196	0	0.686	0.0165	0.140	0.158	0.1834	0.8166
2	0.702	4.10E−3	3.70E−2	1187	1189	0	0.642	0.0463	0.183	0.129	0.1862	0.8138
3	0.652	4.10E−3	3.67E−2	1201	1204	0	0.760	0.0108	0.0672	0.162	0.1796	0.8204

Table 3
Property parameters of components of cell [7–9,17,19,25].

Cell component	Porosity (%)	Tortuosity	Permeability ($m^2\ Pa^{-1}\ s^{-1}$)	Thermal ($W\ m^{-1}\ K^{-1}$)	Density ($kg\ m^{-3}$)	Specific heat ($kJ\ kg^{-1}\ K^{-1}$)
Anode	46	4.5	1.7×10^{-10}	6.2	6200	0.65
Cathode	46	3.0	1.7×10^{-10}	9.6	6000	0.9
Electrolyte	–	–	–	2.7	5560	0.3
Interconnect	–	–	–	9.6	7700	0.8

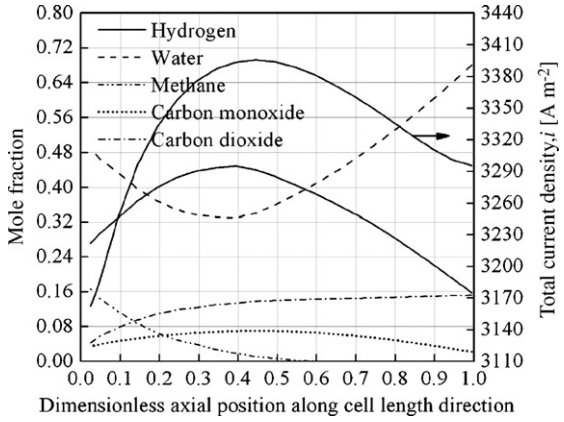

Fig. 4. Species mole fractions in fuel channel, and total current density i along the cell length direction.

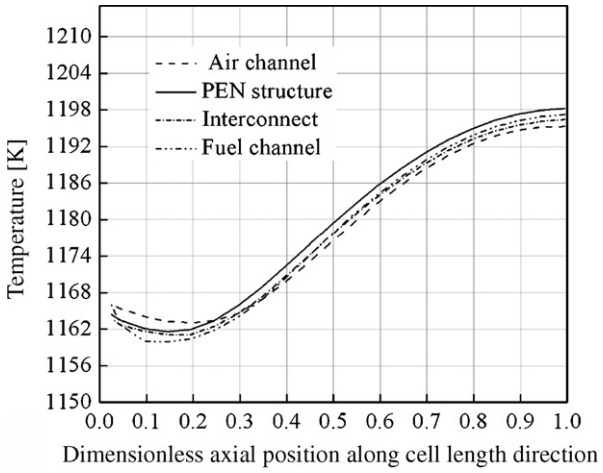

Fig. 5. Gas and air channels, PEN structure, and interconnect temperature along the cell length direction.

the high methane content, the reforming reactions are much faster and the methane is consumed rapidly with the production of H_2 and CO. Once most of the methane is consumed, the H_2 and CO oxidation reactions become the faster reactions, and the consumption of H_2 and CO and production of H_2O and CO_2 can be seen clearly. The total current density profile along the cell length corroborates the increasing electrochemical reactions along the cell length direction, and the location of the maximum total current density almost agrees with that of the maximum H_2 and CO concentrations.

Fig. 5 presents profiles of the fuel and air channels, PEN structure and interconnect temperature along the cell length direction. It is found that the cell temperature decreases in the area close to the cell entrance along the cell length direction, which is because the steam reforming reaction is strongly endothermic. Therefore, the inlet temperature is lowered by the endothermic steam reforming reaction. In the rest areas, the temperature increases along the cell length due to the heat produced by the electrochemical reactions.

Figs. 6 and 7 show the predicted voltage and current density along the cell length, as well as the individual contribution of various potential losses. The potential loss and current density distribution along the cell are related to the composition of the gas streams and to various temperatures in the cell. The electromotive forces, which is defined in the Nernst equations (Eqs. (28) and (29)), is governed by both the cell temperature and the partial pressure of hydrogen and carbon monoxide. In the H_2 oxidation electrochemical model (Eq. (38)), the cathode overpotentials account for 60% of the total losses within the cell, followed by the anode overpotentials for 32%, and the PEN structure ohmic losses for 8%. In the carbon monoxide oxidation electrochemical model (Eq. (39)), the cathode overpotentials account for 77% of the total losses within the cell, followed by the anode overpotentials for 14%, and the PEN structure ohmic losses for 9%. The results above show that reducing the cathode overpotential loss can rapidly improve the total current density in the cell and improve the cell performance. Along the cell length direction, $i_{hyd-oxy}$ increases, while i_{co-oxy} decreases. The phenomenon shows that along the cell length direction, $i_{hyd-oxy}$ accounts for an increasing proportion in the total current density. However, i_{co-oxy} cannot

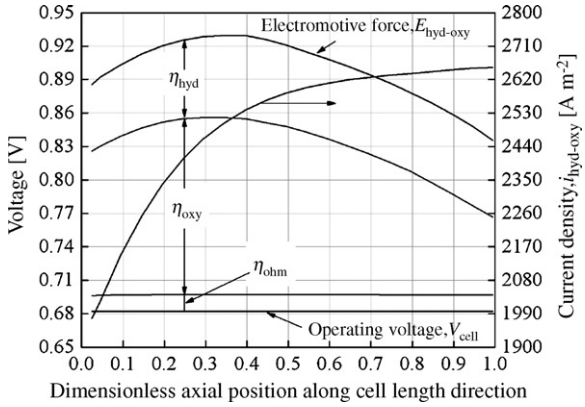

Fig. 6. Predicted voltage, current density $i_{hyd-oxy}$,and the various potential losses along the cell length direction in the hydrogen oxidation reaction.

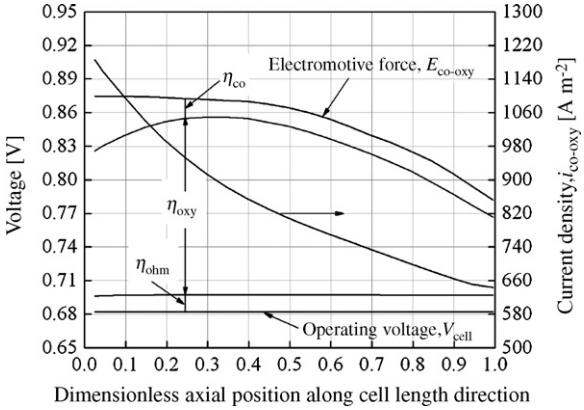

Fig. 7. Predicted voltage, current density i_{co-oxy}, and the various potential losses along the cell length direction in the carbon monoxide oxidation reaction.

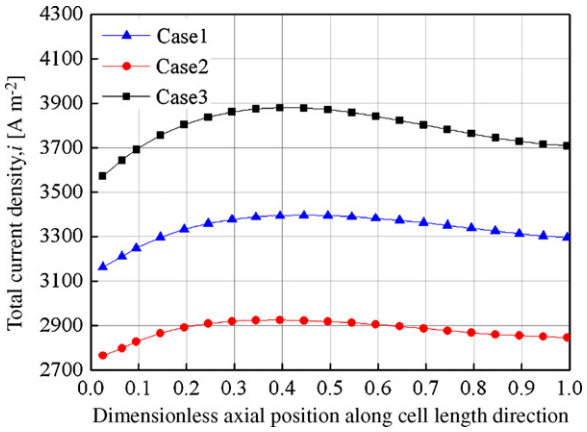

Fig. 8. Predicted total current density i along the cell length direction for all the cases in Table 2.

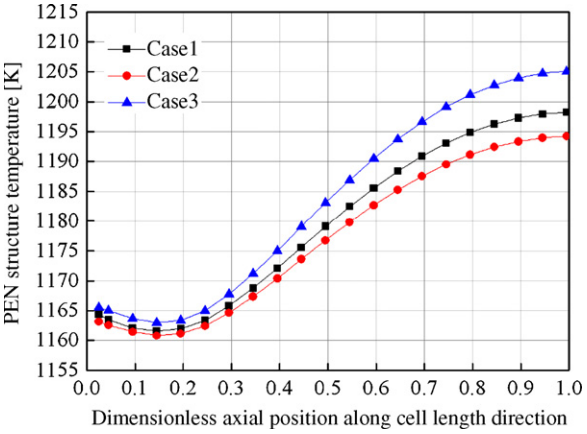

Fig. 9. PEN structure temperature along the cell length direction for all the cases in Table 2.

be ignored. In the operating condition of case1 given in Table 2, it accounts for 18.5% of the total current density, where, the total current density is 3332 A m^{-2}, $i_{hyd-oxy}$ is 2715 A m^{-2}, and i_{co-oxy} is 617 A m^{-2}.

Figs. 8 and 9 and Table 4 illustrate the performance data of the cell under different operating voltages. Fig. 8 shows the total current density profile along the length direction for all the three cases given in Table 2. It is found that the total current density decreases with the increase of the operating voltage. According to the electrochemical model (Eqs. (38) and (39)), all the overpotential losses decrease with the increase of the operating voltage, therefore, all the current densities decrease with the decrease in the overpotential losses. Because the electromotive forces remain almost unchanged and there is direct proportion relationship between the current densities and the overpotential losses under the conditions of the same operating temperature and fuel and air inlet flow rates.

Fig. 9 shows the PEN structure temperature profile along the length direction for all the three cases given in Table 2. It can be seen that the PEN structure temperature decreases with the increase of operating voltage. This is due to the decrease in the heat produced by the electrochemical reactions.

Table 4 shows the performance data of the cell for the cases given in Table 2 in details. All the parameters (except voltage) remain the same. When the operating voltage increases from 0.682 to 0.702 V, the total current density reduces from 3332 to 2870.5 A m^{-2}. Fuel utilization factor and fuel efficiency decrease from 83.6% and 51.0% to 72.0% and 45.5%, respectively. Meanwhile, the air ratio increases from 6.4 to 8.8 with the decrease in total current density. With the changes of the current densities and the air ratio, the average temperature and maximum temperature difference of PEN structure decrease from 1179.2 and 36.6 K to 1176.9 K and 33.2 K, respectively. This is because of less heat produced by the electrochemical reactions and stronger cooling effect of air. The power density of the cell reduces from 2272.4 to 2015.1 W m^{-2}. On the contrary, when the operating voltage reduces from 0.682 V to 0.652 V, the total current density increases from 3332.0 to 3783.3 A m^{-2}. As the total current density increases, fuel utilization factor and fuel efficiency increase from 83.6% and 51.0% to 94.9% and 55.7%, respectively, while the air ratio decreases from 6.4 to 5.7. With the above changes of the current densities and air ratio, the average temperature and maximum temperature difference of PEN structure increase from 1179.2 and 36.6 K to 1183.2 and 42.2 K, respectively, which is unfavorable to the cell. Temperature gradients in a solid oxide fuel cell stack (along the cell length and across the various layers) need to be carefully monitored to avoid any thermally inducing fractures on its ceramic components leading to cell failure. The power density of the cell increases from 2272.4 to 2466.7 W m^{-2}, which is also favorable to the cell. However, the power output of the cell becomes very small if the cell works in a very low operating voltage due to the large overpotential losses. A typical SOFC unit works under the voltage ranging from 0.6 to 0.8 V.

Where i_{max} and i_{min} are the maximum current density and the minimum current density in the cell unit. The maximum current density difference Δi is described as $\Delta i = i_{max} - i_{min}$. T_{ave}, T_{max} and T_{min} are the average temperature, maximum temperature, and maximum temperature of the PEN structure, respectively. The maximum temperature difference of the PEN structure ΔT is described as $\Delta T = T_{max} - T_{min}$.

Tables 5 and 6 show the results for mass heat balance analysis of the coupled model for all the cases in Table 2. The mass production/consumption rate of air and fuel is the difference of mass flow rate between the outlet of air channel and fuel channel and inlet of air channel and fuel channel, respectively. The

Table 4
Performance data of the cell for all the cases in Table 2.

Case	U_f (%)	λ_{air} (%)	P_{SOFC} (W m^{-2})	ε_{SOFC} (%)
1	83.6	6.4	2272.4	51.0
2	72.0	8.8	2015.1	45.5
3	94.9	5.7	2466.7	55.7

Case	i_{ave} (A m^{-2})	i_{max} (A m^{-2})	i_{min} (A m^{-2})	ΔI (A m^{-2})
1	3332.0	3395.3	3162.1	233.2
2	2870.5	2925.2	2765.8	159.4
3	3783.3	3880.4	3573.0	307.4

Case	T_{ave} (K)	T_{max} (K)	T_{min} (K)	ΔT (K)
1	1179.2	1198.2	1161.6	36.6
2	1176.9	1194.2	1161.0	33.2
3	1183.2	1205.1	1162.9	42.2

Table 5
Results for mass balance analysis of the coupled model for all the cases in Table 2.

Cases	Mass production rate of fuel (g h^{-1})	Mass consumption rate of air (g h^{-1})	Mass production/consumption rate based on charge-mass conservation (g h^{-1})
1	3.674E−2	3.972E−2	3.978E−2
2	3.207E−2	3.424E−2	3.427E−2
3	4.170E−2	4.510E−2	4.517E−2

Table 6
Results for heat balance analysis of the coupled model for all the cases in Table 2.

Cases	Reforming heat release rate (W)	Total overpotential heat release rate (W)	Total electrochemical heat release rate (W)	Net heat release rate (W)	Power output (W)
1	−0.0320	0.0273	0.0851	0.0531	0.0908
2	−0.0327	0.0266	0.0782	0.0455	0.0806
3	−0.0314	0.0287	0.0931	0.0617	0.0987

Table 7
Computational parameters for two calculated cases in a H_2–H_2O system and a CO–CO_2 system.

Cases	Flow	Inlet gas delivery		Inlet temperature		Fuel inlet composition				Fuel inlet composition		Operating
	Pattern	n_f^{in} (mol h^{-1})	n_a^{in} (mol h^{-1})	T_{air}^{in} (K)	T_{fuel}^{in} (K)	$y_{H_2O}^{in}$	y_{CO}^{in}	$y_{H_2}^{in}$	$y_{CO_2}^{in}$	$y_{O_2}^{in}$	$y_{N_2}^{in}$	voltage (V)
4	Co-flow	3.05E−3	3.81E−2	1173	1173	0.4	0	0.6	0	0.21	0.79	0.60–0.80
5	Co-flow	3.05E−3	3.81E−2	1173	1173	0	0.6	0	0.4	0.21	0.79	0.58–0.78

mass production/consumption rate based on charge-mass conservation is calculated on basis of Eqs. (11)–(13). It is found that the mass production/consumption rate of air and fuel increase with the decreases of operating voltage because of the mass production/consumption rate of electrochemical reactions increases with the decrease of operating voltage. Comparisons of the mass production/consumption rate of air and fuel and the mass production/consumption rate based on charge-mass conservation, It can be seen that the difference of the two mass production/consumption rates is small for the three cases shown in Table 2. It is validated that the relative error between the mass production/consumption rate of air and the mass production/consumption rate based on charge–mass conservation is less 0.15%, and the relative error between the mass production/consumption rate of fuel and the mass production/consumption rate based on charge-mass conservation is less 7.6% for the three cases shown in Table 2. The precision of mass balance in air channel is much higher than that in fuel channel due to the thin porous electrode. The stagnancy of the species diffusion in the thick anode delays the transport of fuel (H_2 and CO) in the fuel channel to the anode-electrolyte interface and products (H_2O and CO_2) at the anode-electrolyte interface to the fuel channel, especially in the conditions of high reaction rate of electrochemical reactions. The difference between the mass production/consumption rate of fuel and the mass production/consumption rate based on charge–mass conservation is found in the direct internal reforming planar solid oxide fuel cell stack model in the reference literature [13]. In the literature, for a co-flow SOFC operating on a 10% pre-reformed methane fuel mixture with 75% fuel utilization, inlet fuel and air temperatures of 1023 K, average current density of 0.5 A cm^{-2}, and an air ratio of 8.5, an output voltage of 0.66 V with a power density of 0.33 W cm^{-2} and a fuel efficiency of 47%, are predicted by Aguiar et al. From the conditions and results of Table 7 and Figs. 6–8 in the literature, the calculated relative error between the mass production/consumption rate of fuel and the mass production/consumption rate based on charge-mass conservation of the coupled model is about 2.0%. The anode thickness in the literature is 1 mm, therefore, the precision of the relative error between the mass production/consumption rate of fuel and the mass production/consumption rate based on charge-mass conservation of the coupled model is higher than the one in the present paper. From Table 6, it is found that the total overpotential heat release rate, total electrochemical heat release rate and net heat release rate increase with the decrease of the operating voltage. Note that the total overpotential heat is a small portion of the total electrochemical heat. The average temperature of PEN structure increases due to an increase of the total electrochemical heat release rate with the decrease of the operating voltage. The negative values of the reforming heat release rate illuminate that the reforming reactions in the anode are holistically endothermic though the water-shift reaction is weakly exothermic. The reforming heat release rate decreases with the decrease of the operating voltage. This is because the reaction rate of water-shift reaction increases with increase of the average temperature of PEN structure. Therefore, the heat released by water-shift reaction increase with the decrease of the operating voltage. The ratio of reforming heat release rate to net heat release rate decreases with the decrease of the operating voltage, and this is the reason why the maximum temperature difference of the PEN structure increase with the decrease of the operating voltage.

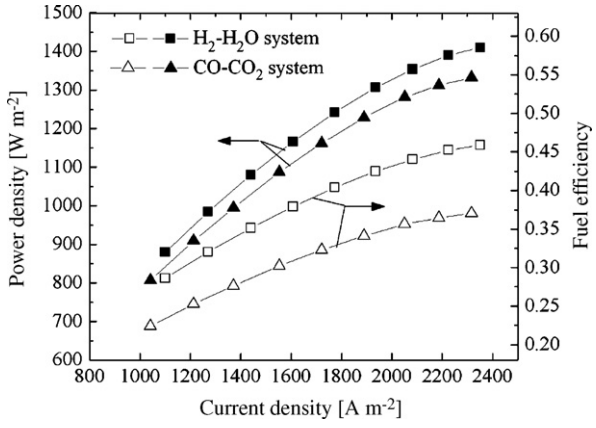

Fig. 10. Comparisons of current-power density and current-fuel efficiency variations in a H_2–H_2O system and a CO–CO_2 system for the two cases in Table 7. The closed symbols and open symbols denote the power density and fuel efficiency, respectively.

In order to research the effect of water-shift reaction on the performance of SOFC, Fig. 10 presents the comparisons of current-power density and current-fuel efficiency variations in a H_2–H_2O system and a CO–CO_2 system for the two cases in Table 7. It can be seen that the power output and fuel efficiency in the H_2–H_2O system are higher than those in CO–CO_2 system under the conditions of same average current density. That is to say, for the same molar consumption of fuel (H_2 and CO), H_2 oxidation reaction gained a higher power output and fuel efficiency relative to CO oxidation reaction. This is illuminated that the water-shift reaction in SOFC system with direct internal reforming of methane can improve the performance of the SOFC in the power output and fuel efficiency. That is because CO is converted into H_2 by water-shift reaction. According above stated, the reaction rate of water-shift reaction increases with the decrease of the operating voltage. Therefore, the power output and fuel efficiency increase with the decrease of the operating voltage. It is validated the predicted results in Table 4.

4. Conclusions

A coupled mathematical model was constructed to study the mass and heat transfer and thermoelectric characteristics of a single cell of SOFCs. Source terms were introduced into the governing equation to describe the variation of mass, momentum and energy in the reaction process. In particular, the momentum source was obtained using the extended Darcy law that took into account the effects of both the viscous force and the inertial force to describe the flow in the porous electrodes.

Based on this model, the performance of SOFC in steady state was analyzed by using CFD code. Major findings from this study are highlighted as follows:

The cathode overpotential loss is the biggest one among all the overpotential losses in the planar anode-supported SOFC, therefore, the reduction of the cathode overpotential loss can rapidly improve the cell's total current density and improve the cell performance. The current density produced by carbon monoxide oxidation reaction cannot be ignored in the direct reforming SOFCs. When the load voltage of the cell decreases, the current densities, fuel utilization factor, fuel efficiency and power density increase, which is favorable to the cell. However, the temperature and temperature gradient of PEN structure also increase, which is unfavorable to the cell. In a word, the operating voltage must be appropriately chosen according to the requirements of practice use to improve the performance of the cell. The water-shift reaction in SOFC system with direct internal reforming of methane can improve the performance of the SOFC in the power output and fuel efficiency through the comparisons of current-power density and current-fuel efficiency variations in a H_2–H_2O system and a CO–CO_2 system under the same working conditions.

Acknowledgement

The authors gratefully acknowledge the contribution of the National Natural Science Foundation of China (Grant No. 30490234).

References

[1] A.L. Dicks, J. Power Sources 71 (1998) 111–122.
[2] I. Mitsunori, H. Takeshi, M. Makoto, et al., Solid State Ionics 132 (2000) 297–308.
[3] H. Yakabe, T. Sakurai, Solid State Ionics 174 (2004) 295–302.
[4] H. Yakabe, Y. Baba, T. Sakurai, et al., J. Power Sources 131 (2004) 278–284.
[5] K.P. Recknagle, R.E. Williford, L.A. Chick, et al., J. Power Sources 113 (2003) 109–114.
[6] N. Autissier, D. Larrain, J. Van herle, et al., J. Power Sources 131 (2004) 313–319.
[7] G. Wang, Y. Yang, H. Zhang, et al., J. Power Sources 167 (2007) 398–405.
[8] Y. Yang, G. Zhang, H. Wang, et al., J. Power Sources 173 (2007) 233–239.
[9] Y. Yang, G. Zhang, H. Wang, et al., J. Power Sources 177 (2008) 426–433.
[10] D. Sánchez, R. Chacartegui, A. Muñoz, et al., J. Power Sources 160 (2006) 1074–1087.
[11] K. Nikooyeh, A.A. Jeje, J.M. Hill, J. Power Sources 171 (2007) 601–609.
[12] J.R. Ferguson, J.M. Fiard, R. Herbin, J. Power Sources 58 (1996) 109–122.
[13] P. Aguiar, C.S. Adjiman, N.P. Brandon, J. Power Sources 138 (2004) 120–136.
[14] B.A. Haberman, J.B. Young, Int. J. Heat Mass Trans. 47 (2004) 3617–3629.
[15] Q. Wang, C. Wang, B. Ren, et al., Energy Eng. 126 (2007) 16–21 (in Chinese).
[16] Q. Wang, B. Ren, L. Li, et al., J. Therm. Sci. Technol. 5 (2006) 339–345 (in Chinese).
[17] H. Yakabe, M. Hishinuma, M. Uratani, et al., J. Power Sources 86 (2000) 423–431.
[18] J. Yuan, B. Sunden, J. Heat Transf. 127 (2005) 1380–1390.
[19] H. Yakabe, T. Ogiwara, M. Hishunuma, et al., J. Power Sources 102 (2001) 144–154.
[20] G.J. van Wylen, R.E. Sonntag, Fundamentals of Classical Thermodynamics, Second ed., John Miley and Sons, Inc., New York, 1985, pp. 683–700.
[21] W. Lehnert, J. Meusinger, F. Thom, J. Power Sources 87 (2000) 57–63.
[22] E. Achenbach, J. Power Sources 49 (1994) 333–348.
[23] R. Suwanwarangkul, E. Croiset, M.W. Fowler, et al., J. Power Sources 122 (2003) 9–18.
[24] S. Christoph, T. Bjorn, Steinar, et al., J. Power Sources 141 (2005) 227–240.
[25] Y. Shiratori, Y. Yamazaki, J. Power Sources 114 (2003) 80–87.